Large-Eddy Simulation of Evaporating Spray

in a Coaxial Combustor

Sourabh V. Apte

School of Mechanical, Industrial and Manufacturing Engineering, Oregon State

University, Corvallis, OR 97331

Krishnan Mahesh

Department of Aerospace Engineering and Mechanics, University of Minnesota,

Minneapolis, MN 55455

Parviz Moin

Center for Turbulence Research, Stanford University, Stanford, CA 94305

Corresponding Author

Sourabh V. Apte, Oregon State University, 204 Rogers Hall, Corvallis, OR 97331,

USA,

email: sva@engr.orst.edu, phone: 541-737-7335, fax: 541-737-2600

Abstract

Large-eddy simulation of an evaporating isopropyl alcohol spray in a coaxial combustor is performed. The Favre-averaged, variable density, low-Mach number Navier-Stokes equations are solved on unstructured grids with dynamic subgrid scale model to compute the turbulent gas-phase. The original incompressible flow algorithm for LES on unstructured grids by Mahesh *et al.* (J. Comp. Phy., 2004, **197**, 215–240) is extended to include density variations and droplet evaporation. An efficient particle-tracking scheme on unstructured meshes is developed to compute the dispersed phase. Experimentally measured droplet size distribution and size-velocity correlation near the nozzle exit are used as the inlet conditions for the spray. The predictive capability of the LES approach on unstructured grids together with Lagrangian droplet dynamics models to capture the droplet dispersion characteristics, size distributions, and the spray evolution is examined in detail. The mean and turbulent quantities for the gas and particle phases are compared to experimental data to show good agreement. It is shown that for low evaporation rates considered in the present study, a well resolved large-eddy simulation together with simple subgrid models for droplet evaporation and motion provides good agreement of the mean and turbulent quantities for the gas and droplet phases compared to the experimental data. This work represents an important first step to assess the predictive capability of the unstructured grid LES approach applied to spray vaporization. The novelty of the results presented is that they establish a baseline fidelity in the ability to simulate complex flows on unstructured grids at conditions representative of gas-turbine combustors.

Key words: Sprays, LES, unstructured grids, particle-laden flows, Eulerian-Lagrangian

1 Introduction

Turbulent multi-phase flows are encountered in a variety of engineering applications; e.g. internal combustion engines, liquid and solid propellant rocket motors, gas-turbine aircraft engines, cyclone combustors, and biomass gasifiers. The physics of such flows is extremely complex. In gas turbine combustors, for example, the liquid fuel jet undergoes primary and secondary atomization, the resulting droplets evaporate/condense and collide/coalesce, fuel and oxidizer then mix yielding spray-flames. In addition, realistic combustor configurations make accurate numerical predictions a challenging task. High-fidelity simulations of these flows require use of accurate numerical schemes with good conservative properties and advanced sub-grid models to capture the physical phenomena associated with both phases. To build a comprehensive numerical approach with good predictive capability for such flows, a systematic development and validation of new schemes and models are necessary. It is also important to investigate limitations of any simplifying assumptions, and their potential impact on the flow evolution. In the present work, emphasis is placed on simulation and analysis of evaporating spray in a coaxial combustion chamber where detailed experimental data together with well-specified boundary conditions are available. The approach is based on large-eddy simulation on unstructured grids [1] with the potential of simulating complex flows in realistic configurations. The predictive capability of this approach with subgrid scale models for spray evaporation is evaluated.

Most numerical investigations of particle-turbulence interactions with large number of particles (on the order of millions) use DNS [2–4], LES [5,6] or RANS [7] for the continuum carrier phase and a 'point-particle (PP)' assumption for the dispersed phase. The dispersed phase is assumed *subgrid* so that the particle size (d_p) is assumed smaller than the Kolmogorov length scale (L_K) for DNS, and d_p is smaller than the grid size (Δ) in LES or RANS. However, in LES (or RANS),

only the spatially filtered, $\overline{\phi} = \phi_f - \phi^{sgs}$ (or time-averaged, $\langle\phi\rangle = \phi_f - \phi'$), flow quantities (fluid velocities, species mass fractions, and temperature) are computed. Effect of the subgrid-scale quantities, ϕ^{sgs} (or ϕ' in RANS) should be modeled to correctly represent the forces on the particle.

Considerable effort has been devoted to reconstruct the effect of unresolved velocity fluctuations ($\mathbf{u}^{sgs}$) on the particle motion using statistical methods, stochastic theory and Langevin models [8,9]. It has been shown that one-point statistics such as particle dispersion, velocity fluctuations, and time-scales are less sensitive to the subgrid-scale velocity fluctuations. For evaporating droplets, *a priori* studies on subgrid scale modeling have also been performed [10]. Reveillon & Vervisch [11] showed that for evaporating sprays, droplet vaporization adds additional unclosed terms in the evaluation of the mixture fraction variance field. Both the scalar dissipation rate and the mixing characteristics are affected, as a result.

Recently, simulations of solid particle-laden turbulent flow by Apte et al. [6], neglected the direct effect of the subgrid velocity fluctuations on particle motion and showed excellent agreement with experimental data. It was found that if the energy content in the subgrid scale is small compared to the resolved scale kinetic energy, the influence of the subgrid velocity is typically negligible. This approach was further extended to model liquid fuel atomization using a stochastic model for secondary breakup and showed good agreement with experimental data [12]. However, evaporating-droplet laden flow was not simulated.

Menon and co-workers [13] have performed large-eddy simulations of non-reacting and reacting flows in a swirling combustion chamber with liquid spray in complex configuration. They showed good predictive capability of LES in capturing spray evolution, droplet dispersion, and turbulence modulation by droplets in the presence of heat release. There approach is based on compressible Navier-Stokes equations in generalized coordinates. In order to represent complex passages in

combustors with relatively easy grid generation, use of unstructured grids is necessary. Mahesh *etal.* [1,14] developed new algorithms for LES of single-phase non-reacting and reacting flows in complex configurations and showed the effectiveness of LES in combustor geometries. In the present work, we extend their formulation for incompressible flows to variable-density flows at low-Mach numbers (as those encountered in gas-turbine combustors) to include physics of droplet vaporization, droplet dispersion, and turbulent mixing of fuel vapor and oxidizer. Emphasis is placed on the predictive capability of a well-resolved LES on unstructured grids to capture the mean and standard deviations in droplet size and velocity distributions.

Sommerfeld et al. [15] provide detailed measurements of an evaporating isopropyl alcohol spray in a model combustion chamber. Detailed measurements of the droplet size distributions very near the injector were performed in addition to one-component phase-Doppler-anemometer (PDA) measurements to obtain mean and rms gas-phase and droplet-phase statistics of velocity and particle size. Since detailed droplet size distributions and size-velocity correlations near the injector nozzle are available, these can be used as inflow conditions for the liquid spray, thus eliminating any uncertainties associated with spray atomization and secondary breakup modeling. RANS-based modeling of this experimental setup with Eulerian-Lagrangian approach [16] and joint-pdf based Eulerian-Eulerian approach [17] have been reported. The RANS simulations [16] indicated strong sensitivity of predicted results to the number of computational parcels used in the simulation. LES study of this test case on unstructured grids has not been conducted and represents an important step to assess the predictive capability of flow solvers specifically developed for complex combustor configurations. Detailed measurements as reported by this experimental study are typically not feasible in realistic geometries and thus this data provides an excellent benchmark case for validating evaporating spray models.

2 Mathematical Formulation

The mathematical formulation is based on the variable density, low-Mach number equations for the fluid phase. Any acoustic interactions and compressibility effects are neglected. In addition, in writing the energy equation, we invoke the low-Mach number assumptions together with unity Lewis number. Also the viscous dissipation and Dufour effects are assumed negligible.

2.1 Gas-Phase Equations

The Favre-averaged governing equations for LES of the low-Mach number, variable density flow are given below,

$$\frac{\partial \overline{\rho_g}}{\partial t} + \frac{\partial \overline{\rho_g} \tilde{u}_j}{\partial x_j} = \overline{\dot{S}_m}, \tag{1}$$

$$\frac{\partial \overline{\rho_g} \tilde{u}_i}{\partial t} + \frac{\partial \overline{\rho_g} \tilde{u}_i \tilde{u}_j}{\partial x_j} = -\frac{\partial \overline{p}}{\partial x_i} + \frac{\partial}{\partial x_j}\left(2\overline{\mu}\tilde{S}_{ij}\right) - \frac{\partial q_{ij}}{\partial x_j} + \overline{\dot{S}_i}, \tag{2}$$

$$\frac{\partial \overline{\rho_g} \tilde{Z}}{\partial t} + \frac{\partial \overline{\rho_g} \tilde{Z} \tilde{u}_j}{\partial x_j} = \frac{\partial}{\partial x_j}\left(\overline{\rho_g}\tilde{\alpha}_Z \frac{\partial \tilde{Z}}{\partial x_j}\right) - \frac{\partial q_{Zj}}{\partial x_j} + \overline{\dot{S}_Z}, \tag{3}$$

$$\frac{\partial \overline{\rho_g} \tilde{h}}{\partial t} + \frac{\partial \overline{\rho_g} \tilde{h} \tilde{u}_j}{\partial x_j} = \frac{\partial}{\partial x_j}\left(\overline{\rho_g}\tilde{\alpha}_h \frac{\partial \tilde{h}}{\partial x_j}\right) - \frac{\partial q_{hj}}{\partial x_j} + \overline{\dot{S}_h}, \tag{4}$$

where $\tilde{S}_{ij} = \frac{1}{2}\left(\frac{\partial \tilde{u}_i}{\partial u_j} + \frac{\partial \tilde{u}_j}{\partial u_i}\right) - \frac{1}{3}\delta_{ij}\frac{\partial \tilde{u}_k}{\partial x_k}$, and $\tilde{\rho}_g$ is the density of the gaseous mixture, $\tilde{Z}$ is the filtered mixture fraction, $\tilde{u}_i$ is the velocity, $\overline{\mu}$ is the viscosity, $\overline{p}$ is the pressure, $h = \sum_i Y_i h_i(T)$ is the total mixture enthalpy, $\dot{S}$ are the source terms due to inter-phase coupling. The subgrid scale unclosed transport terms in the momentum, scalar, and enthalpy equations are grouped into the residual stress q_{ij}, and residual scalar flux q_{Zj}, q_{hj}. The dynamic Smagorinsky model by Moin et al. [18,19] is used. The dynamic model has no adjustable constants, and thus allows evaluation of the predictive capability of the model.

For the present study, no chemical reactions are considered and chemical source terms are absent. The liquid droplets evaporate and the resulting fuel vapor undergoes pure mixing with the surrounding air. Unlike a two-inlet pure gaseous system, the fuel in the above formulation is in the liquid form. This implies that the maximum value of vapor fuel mass fraction is dependent on the local saturation conditions around a drop.

The source terms in the gas-phase continuity, mixture-fraction, and momentum equations are obtained from the equations governing droplet dynamics (Eqs. 8, 9). For each droplet the source terms are interpolated from the particle position $(\mathbf{x_p})$ to the centroid of the grid control volume using an interpolation operator. The source terms in the continuity and mixture fraction equations are identical as they represent conservation of mass of fuel vapor. The expressions for source terms are:

$$\overline{\dot{S}_m}(\mathbf{x}) = \overline{\dot{S}_Z}(\mathbf{x}) = -\sum_k \mathcal{G}_\sigma(\mathbf{x}, \mathbf{x_p}) \frac{d}{dt}(m_p) \tag{5}$$

$$\overline{\dot{S}_i}(\mathbf{x}) = -\sum_k \mathcal{G}_\sigma(\mathbf{x}, \mathbf{x_p}) \frac{d}{dt}\left(m_p u_{pi}^k\right) \tag{6}$$

$$\overline{\dot{S}_h}(\mathbf{x}) = -\sum_k \mathcal{G}_\sigma(\mathbf{x}, \mathbf{x_p}) \frac{d}{dt}(m_p C_{p,\ell} T_p) \tag{7}$$

where the summation is over all droplets (k). The function $\mathcal{G}_\sigma$ is a conservative interpolation operator with the constraint $\int_{V_{cv}} \mathcal{G}_\sigma(\mathbf{x}, \mathbf{x}_p) dV = 1$ [6], and V_{cv} is the volume of the grid cell in which the droplet lies.

2.2 Liquid-Phase Equations

Droplet dynamics are simulated using a Lagrangian point-particle model. It is assumed that (1) the density of the droplets is much greater than that of the carrier fluid, (2) the droplets are

dispersed and collisions between between them are negligible, (3) the droplets are much smaller than the LES filter width, (4) droplet deformation effects are small, and (5) motion due to shear is negligible. Under these assumptions, the Lagrangian equations governing the droplet motions become [20]

$$\frac{d\mathbf{x}_p}{dt} = \mathbf{u}_p; \quad \frac{d\mathbf{u}_p}{dt} = \frac{1}{\tau_p}\left(\mathbf{u}_{g,p} - \mathbf{u}_p\right) + \left(1 - \frac{\rho_g}{\rho_p}\right)\mathbf{g} \tag{8}$$

where $\mathbf{x}_p$ is the position of the droplet centroid, $\mathbf{u}_p$ denotes the droplet velocity, $\mathbf{u}_{g,p}$ the gas-phase velocities interpolated to the droplet location, ρ_p and ρ_g are the droplet and gas-phase densities, and $\mathbf{g}$ is the gravitational acceleration. The droplet relaxation time scale (τ_p) is given as: $\tau_p = \rho_p d_p^2/[18\mu_g(1 + aRe_p^b)]$, where d_p is the diameter and $Re_p = \rho_g d_p|\mathbf{u}_{g,p} - \mathbf{u}_p|/\mu_g$ is the droplet Reynolds number [20]. The above correlation is valid for $Re_p \leq 800$. The constants $a = 0.15, b = 0.687$ yield the drag within 5% from the standard drag curve. It should be noted that these assumptions are valid in regions of dilute spray where the droplet size is smaller than the LES filter width. Near the injector the droplets are densely packed, and undergo collision and coalescence. In addition, the grid resolution may become comparable to droplet size. Under these assumptions, the point-particle approach is not valid. Recently, Apte *et al.* [21] investigated a mixture-theory based model taking into account the volumetric displacements in dense particulate flows to show significant influences on the flow field. In the present simulation, the spray breakup process is not simulated, the droplet size distribution measured in the experiments is used as an inlet condition, and further away from the injection point, the spray becomes dilute. However, a model taking into account the volumetric fluid displacement caused by droplet motion should be considered in regions of dense spray.

The droplet evaporation is modeled based on an equilibrium 'uniform-state' model for an isolated droplet [22–24]. Miller et al [25] investigated different models for evaporation accounting for non-

equilibrium effects. In the present work, non-equilibrium effects are neglected since the rates of evaporation are slow for the low gaseous temperatures used in the experiment. Advanced models considering internal circulation, temperature variations inside the droplet, effects of neighboring droplets [24] may alter the heating rate (Nusselt number) and the vaporization rates (Sherwood number). However, for the present case of non-reacting flow, the evaporation is dominated by mass-diffusion, the rates are low, and hence these effects are neglected. The Lagrangian equations governing droplet temperature and mass become [22–24]

$$\frac{dm_p}{dt} = -\frac{m_p}{\tau_m}; \quad \frac{dT_p}{dt} = \frac{1}{\tau_c}\left(T_{g,p} - T_p^s\right) - \frac{1}{\tau_m}\frac{\Delta h_v}{C_{p,\ell}} \tag{9}$$

where Δh_v is the latent heat of vaporization, m_p mass of the droplet, T_p temperature of the droplet, T_p^s is the temperature at the droplet surface, $T_{g,p}$ is the temperature of the gas-phase at the droplet location and $C_{p,\ell}$ is the specific heat of liquid. The diameter of the droplet is obtained from its mass, $d_p = (6m_p/\pi\rho_p)^{1/3}$. Here, τ_m and τ_c are the droplet life-time and the convective heating time-scales respectively, and are given as

$$\frac{1}{\tau_m} = \frac{12}{d_p^2}\mathcal{D}^s\ln(1 + B_Y)\text{Sh}; \quad \frac{1}{\tau_c} = \frac{12}{\rho_p d_p^2}\frac{k^s}{C_{p,\ell}}\frac{\ln(1 + B_T)}{B_T}\text{Nu}. \tag{10}$$

Here, $\mathcal{D}$ and k are the diffusivity and conductivity, respectively. The superscript s stands for droplet surface and Sh and Nu are the Sherwood and Nusselt numbers given as

$$\text{Sh} = 1 + \frac{0.278Re_p^{1/2}[Sc^s]^{1/3}}{\sqrt{1 + 1.232/Re_p[Sc^s]^{1/3}}}; \quad \text{Nu} = 1 + \frac{0.278Re_p^{1/2}[Pr^s]^{1/3}}{\sqrt{1 + 1.232/Re_p[Pr^s]^{1/3}}}. \tag{11}$$

B_Y and B_T are the mass diffusion and heat transfer coefficients, respectively. For $T_p^s < T_b$ (where T_b is the boiling point), $B_Y = (Y_F^s - Y_{Fg,p})/(1 - Y_F^s)$ and $B_T = C_p^s(T_{g,p} - T_p^s)/(\Delta h_v)$, where $Y_{Fg,p}$ is the fuel vapor mass-fraction interpolated to the droplet location. For $T_p^s \geq T_b$, B_Y is set equal to B_T. The Clausius-Clapeyron equilibrium vapor-pressure relationship is used to compute the

fuel mass-fraction at the droplet surface. Liquid properties are evaluated using the $1/3^{rd}$ rule for reference mass fractions [22].

2.3 Subgrid Scale Modeling

In LES of droplet-laden flows, the droplets are presumed to be *subgrid*, and the droplet-size is smaller than the filter-width used. The gas-phase velocity field required in Eq. (8) is the total (unfiltered) velocity, however, only the filtered velocity field is computed in Eqs. (2). The direct effect of unresolved velocity fluctuations on droplet trajectories depends on the droplet relaxation time-scale, and the subgrid kinetic energy. Pozorski & Apte [8] performed a systematic study of the direct effect of subgrid scale velocity on particle motion for forced isotropic turbulence. It was shown that, in poorly resolved regions, where the subgrid kinetic energy is more than 30%, the effect on droplet motion is more pronounced. A stochastic model reconstructing the subgrid-scale velocity in a statistical sense was developed [8]. However, in well resolved regions, where the amount of energy in the subgrid scales is small, this direct effect was not strong. In the present work, the direct effect of subgrid scale velocity on the droplet motion is neglected. However, note that the particles *do feel* the subgrid scales through the subgrid model that affects the resolved velocity field. For well-resolved LES of swirling, separated flows with the subgrid scale energy content much smaller than the resolved scales, the direct effect was shown to be small [6].

In addition, work by Masoudi and Sirignano [26] has shown that collisions between subgrid scale vortices and droplet sizes can modify the Nusselt and Sherwood numbers used in convective correction factors (Eq. 10). In the present case the evaporation rates are low and are not significantly affected by these effects. However, in general these effects need to be investigated in the context

10

of LES.

To account for the effects of the SGS turbulence, the filtered mass fractions and temperature fields are correlated with the mixture fraction, $\tilde{Y}_i = \tilde{Y}_i(\tilde{Z}, \widetilde{Z''^2})$. In the present work, a presumed beta-pdf approach is used to evaluate the filtered mass-fraction fields:

$$\tilde{Y}_i = \int Y_i(\zeta)P_Z(\zeta)d\zeta; \quad P_Z(\zeta) = \frac{\zeta^{a-1}(1-\zeta)^{b-1}}{\int_0^1 \zeta^{+a-1}(1-\zeta^+)^{b-1}d\zeta^+}; \tag{12}$$

where $a = \frac{\tilde{Z}}{\tilde{Z}^s}\left(\frac{(\tilde{Z}/\tilde{Z}^s)(1-\tilde{Z}/\tilde{Z}^s)}{\widetilde{Z''^2}/(\tilde{Z}^s)^2} - 1\right)$ and $b = a\left(\frac{1}{\tilde{Z}/\tilde{Z}^s} - 1\right)$. Here, Z^s is the local saturation mixture fraction and is obtained by averaging the surface values of fuel mass fractions over all droplets in a given control volume. The beta pdf used here ensures that P_Z is properly defined in the range $0 \leq Z \leq Z^s$ [11]. The mixture fraction variance $\widetilde{Z''^2}$ is modeled as $\bar{\rho}\widetilde{Z''^2} = \mathcal{C}_Z\bar{\rho}\Delta^2|\nabla\tilde{Z}|^2$, where Δ is the filter width, and the coefficient $\mathcal{C}_Z$ is obtained using the dynamic procedure [19]. This implicitly assumes that the time-scale of evaporation is small compared to the scalar mixing time-scale. However, use of more advanced micro-mixing models [11] may become necessary in the presence of chemical reactions.

3 Numerical Method

The computational approach is based on a co-located, finite-volume, energy-conserving numerical scheme on unstructured grids [14] and solves the low-Mach number, variable density gas-phase flow equations. Numerical solution of the governing equations of continuum phase and particle phase are staggered in time to maintain time-centered, second-order advection of the fluid equations. Denoting the time level by a superscript index, the velocities are located at time level t^n and t^{n+1}, and pressure, density, viscosity, and the scalar fields at time levels $t^{n+3/2}$ and $t^{n+1/2}$. Droplet position, velocity and temperature fields are advanced explicitly from $t^{n+1/2}$ to $t^{n+3/2}$

11

using fluid quantities at time-centered position of t^{n+1}. In this co-located scheme, the velocity and pressure fields are stored and solved at the centroids of the control volumes.

Lagrangian droplet equations:

The droplet equations are advanced using a third-order Runge-Kutta scheme. Owing to the disparities in the flowfield time-scale (τ_f), the droplet relaxation time (τ_p), the droplet evaporation time-scale (τ_m), and the droplet heating time-scale (τ_c), sub-cycling of the droplet equations becomes necessary. Accordingly, the time-step for droplet equation advancement (Δt_p) is chosen as the minimum of the these time scales and the time-step for the flow solver (Δt). As the droplet size becomes very small, Δt_p reduces, and each droplet equation is solved multiple times per time-step, giving good temporal resolution to capture doplet dispersion within a time-step.

Especially, care needs to be taken as the droplet diameter becomes very small due to evaporation. Under these conditions, the time scales associated with the droplet velocity, size, or the droplet heating may become much smaller than the flow solver time-step. The fluid flow solution, then is assumed locally frozen (or constant), and the ordinary differential equations are integrated analytically [27]. The droplet mass, velocity, and temperature are then given by the following analytical expressions: $m_p(t) = m_p(t^0) \left[1 - \Delta t_p/\tau_\ell \right]$; $\mathbf{u}_p(t) = \mathbf{u}_{g,p}(t) - (\mathbf{u}_{g,p} - \mathbf{u}_p)^0 \exp\left[-\Delta t_p/\tau_p \right]$; $\theta(t) - \frac{\tau_c}{\tau_\ell} \frac{\Delta H_v}{C_{p,\ell}} = \left[\theta(t^0) - \frac{\tau_c}{\tau_\ell} \frac{\Delta H_v}{C_{p,\ell}} \right] \exp\left(-\Delta t_p/\tau_c \right)$, where m_p is mass of the droplet, $\theta = T_{g,p} - T_p$, and the superscript 0 stands for solution at an earlier time level.

Locating the droplet:

After obtaining the new droplet positions, the droplets are relocated, droplets that cross interprocessor boundaries are duly transferred, boundary conditions on droplets crossing boundaries are applied, source terms in the gas-phase equation are computed, and the computation is further advanced. Solving these Lagrangian equations thus requires addressing the following key issues: (i) efficient search for locations of droplets on an unstructured grid, (ii) interpolation of gas-phase properties to the droplet location for arbitrarily shaped control volumes, (iii) inter-processor droplet transfer.

Locating droplets in a generalized-coordinate structured code is straightforward since the physical coordinates can be transformed into a uniform computational space. This is not the case for unstructured grids. The approach used in this work, projects the droplet location onto the faces of the control volume and compares these vectors with outward face-normals for all faces. If the droplet lies within the cell, the projected vectors point the same way as the outward face-normals. This technique is found to be very accurate even for highly skewed elements. A search algorithm is then required to efficiently select the control volume to which the criterion should be applied.

An efficient technique termed as 'the known vicinity algorithm' was used to identify the control volume number in which the droplet lies. Given a good initial guess for a droplet location, the known-vicinity algorithm identifies neighboring grid cells by traversing the direction the droplet has moved. In LES, the time steps used are typically small in order to resolve the temporal scales of the fluid motion. The droplet location at earlier time-steps provide a very good initial guess. Knowing the initial and final location of the droplet, this algorithm searches in the direction of the droplet motion until it is relocated. The neighbor-to-neighbor search is extremely efficient if the droplet is located within 10-15 attempts, which is usually the case for 95% of the droplets in the

present simulation. Once this cell is identified, the fluid parameters are interpolated to the droplet location using a conservative Gaussian kernel, which makes use of values at nearest neighboring cells. Similarly, the interaction terms from the droplets to the carrier fluid equations make use of the same interpolation function. This droplet tracking algorithm is efficient and can locate droplets on complex unstructured grids allowing simulation of millions of droplet trajectories. In the present case, droplets are distributed over several processors used in the computation, and the load-imbalance is not significant. Details of the algorithm are given in Apte et al. [6].

Advancing the fluid flow equations:

The scalar fields (fuel mass fraction, and enthalpy) are advanced using the old time-level velocity field. A second-order WENO scheme is used for scalar advective terms and centered differencing for the diffusive terms. All terms, except the inter-phase source terms, are treated implicitly using Crank-Nicholson for temporal discretization. Once the scalar fields are computed, the density and temperature fields are obtained from constitutive relations and ideal gas law. The cell-centered velocities are advanced in a predictor step such that the kinetic energy is conserved. The predicted velocities are interpolated to the faces and then projected. Projection yields the pressure potential at the cell-centers, and its gradient is used to correct the cell and face-normal velocities. The steps involved in solving the projection-correction approach for velocity field are described below:

- Advance the fluid momentum equations using the fractional step algorithm. The density field is available at intermediate time level is obtained from arithmetic average at the two time steps $t^{n+3/2}$ and $t^{n+1/2}$.

$$\frac{\rho u_i^* - \rho u_i^n}{\Delta t} + \frac{1}{2V_{cv}} \sum_{\text{faces of cv}} \left[u_{i,f}^n + u_{i,f}^* \right] g_N^{n+1/2} A_f = \tag{13}$$

14

$$\frac{1}{2V_{cv}} \sum_{\text{faces of cv}} \mu_f \left(\frac{\partial u_{i,f}^*}{\partial x_j} + \frac{\partial u_{i,f}^n}{\partial x_j} \right) A_f + F_i^{n+1}$$

where f represents the face values, N the face-normal component, $g_N = \rho u_N$, and A_f is the face area. The superscript '$*$' represents the predicted velocity field.

- Interpolate the velocity fields to the faces of the control volumes and solve the Poisson equation for pressure:

$$\nabla^2 (p\Delta t) = \frac{1}{V_{cv}} \sum_{\text{faces of cv}} \rho_f u_{i,f}^* A_f + \frac{\rho^{n+3/2} - \rho^{n+1/2}}{\Delta t} \qquad (14)$$

- Reconstruct the pressure gradient, compute new face-based velocities, and update the cv-velocities using the least-squares interpolation used by Mahesh *et al.* [1]:

$$\frac{\rho \left(u_i^{n+1} - u_i^* \right)}{\Delta t} = -\frac{\delta p}{\delta x_i} \qquad (15)$$

4   Computational Details

Figure 1 shows a schematic of the computational domain used for the model coaxial combustor investigated by Sommerfeld & Qiu [15]. The chamber consists of an annular section discharging hot air into a cylindrical test section with sudden expansion. A large stagnation region is attached at the end of the test section so that convective outflow conditions can be applied. Gravity acts in the axial direction. In the experiments, the central section consists of a nozzle through which isopropyl alcohol at 313 K is sprayed into the test section. Hot air at constant temperature of 373 K enters the annulus. The boiling temperature of isopropyl alcohol at atmospheric pressures is 355 K and thus the evaporation is dominated by mass transfer effects. The air and liquid mass flow rates are 28.3 and 0.44 g/s, respectively. The overall mass-loading is small resulting in a dilute spray.

The outer radius of the annulus (R = 32 mm) is taken as the reference length scale (L_{ref}) with which the computational domain and flow parameters are scaled. The average axial inlet velocity (U_{ref}) in the annular section is 15.47 m/s. Based on the reference length scale, the average inlet velocity, and the density and viscosity of the hot air, the reference Reynolds number is 21164. For a given mass-flow rate, the turbulent velocity components in the annular pipe section are obtained using the body-force technique developed by Pierce and Moin [28]. This inflow data over several flow through times is generated *a priori* and read at each time step to specify the velocity components at the inlet. Convective boundary conditions are applied at the exit section by conserving the global mass flow rate through the combustor. No-slip conditions are enforced at the walls. In this work, we use the dynamic subgrid model which can be integrated all the way to the wall. The wall is therefore resolved and no wall-model is used. Adiabatic conditions are used at the test-section walls.

Figure 2 shows the computational grid used. The computational domain is divided into approximately 1.5×10^6 hexahedral volumes, with around 0.7×10^6 elements clustered in the test section near the injector (x/R $\leq$ 15). As shown in Fig. 2b, the central region of the primary jet consists of a quad mesh which eliminates the coordinate singularity point commonly observed in axisymmetric structured grids near the centerline. The smallest grid spacing is around 20 μm near the walls and in the shear layers with steep velocity gradients close to the annular inlet into the test-section. The computational domain is partitioned amongst 64 processors.

The mass-flow rate and inlet droplet diameter distribution determines the number of droplets to be injected per time step. Experimental data very near the injection section (x/R = 0.09375) is used as inlet condition for the liquid phase. The droplet size distributions at different radial locations (grouped into 10 radial zones of size 1 mm) were measured. A log-normal distribution was used as a curve-fit for each radial zone. In addition, the joint pdf of droplet size-velocity is

also available at the inlet. To inject droplets from the central section, first a location is sampled over a radial span of ± 10 mm around the center. Knowing the droplet location the droplet size distribution, corresponding to the radial zone containing the droplet, is chosen and a droplet diameter is sampled. Knowing the droplet diameter, the velocities are obtained from the size-velocity joint pdf and is used as the inlet velocity. This also determines the angle at which the droplet will enter the test section. In the present LES computation, *each droplet is tracked* until it either completely evaporates or exits the test section at $x/R = 15$. This yields around 1×10^6 droplets in the domain at stationary state. The overall computational time is less than 72 CPU-hours on the IBM cluster at the San Diego Supercomputing center.

5   Results and Discussion

First, the single-phase air flow through the model combustion chamber is simulated (without injecting any liquid droplets). The radial variations of the mean and *rms* axial velocity field at different axial locations are compared with the experimental data (not shown, see supplementary data). Similar predictions are obtained for the radial velocity fields. In this single-phase simulation, the only input is the inlet mean mass flow rate. The inflow data generated based on the mean Reynolds number is applied to the inlet section at each time step. Such detailed treatment of the inlet boundary conditions together with the dynamic subgrid scale models facilitates true prediction of the flow field without any tunable model constants. The high axial flux through the annular section enters the sudden expansion region, and results in a recirculation region and shear layers that are captured well by the present LES.

Liquid droplets are then injected through the central section following the procedure described before. Figure 3 shows the snapshot of the fuel vapor mass fraction superimposed with droplet

scatter plot in the z = 0 plane. Initially as the droplets are injected into a pure air flow, they evaporate quickly due to strong gradients in mass fraction fields. The fuel vapor then mixes with hot air and the mixture temperature is reduced. The incoming new droplets thus see reduced temperatures and evaporate at a slower rate and travel a longer distance downstream. A stationary state is reached at which the inlet liquid mass flux is balanced by the exit liquid and fuel vapor flux. The liquid-phase statistics are then initiated and collected over a few flow through time scales.

Figures 4a–b show the radial variations of the mean and rms fluctuations in the axial velocity fields for the liquid droplets. These statistics are obtained by ensemble averaging over all droplet sizes. Averaging over several flow through times is thus necessary to accurately predict the droplet behavior. Just downstream of the nozzle, the maximum mean axial velocity of the droplets is around 15 m/s. These droplets move downstream and spread radially outward. The recirculation region developing downstream of the nozzle section results in negative droplet mean axial velocities in the core of the spray at x/R = 0.786. The highest liquid flux exists on the edge of the spray. As the liquid droplets move downstream, they are carried by the hot air and their axial velocity exhibits similar behavior as that of the gaseous phase.

Figures 5a–b show the mean and rms droplet diameters (D_{10}–distribution) at different axial locations. Again the computational predictions match well with the experimental data at all locations. The size distributions are typical of hollow cone atomizer wherein smaller size droplets are entrained in the core, whereas the larger droplets travel to the edge of the spray. The droplet evaporation and turbulent dispersion is well represented by the LES solver and the sub-grid models used. As the droplets move downstream they evaporate, and the radial distribution of the mean diameter becomes more uniform. The profiles of the standard deviation in droplet size indicate a narrow distribution in the core and wide size distributions on the edge of the spray.

Finally, figure 6 shows the variation in the droplet axial mass flux at different axial locations. The maximum axial flux decreases as we move in the downstream direction indicating evaporation. Again good agreement is obtained at all locations. Again two peaks characterizing the hollow cone spray is visible. These peak spread radially making roughly a 60° cone angle. Further downstream, the spreading of the spray is hindered by the entrainment of the annular air jet and the maximum mass-flux shifts to the core region.

6 Summary and Conclusions

A large-eddy simulation of evaporating liquid spray in a model coaxial combustor was performed under the under conditions corresponding to an experiment by Sommerfeld & Qiu [15]. The variable density, low-Mach number equations for non-reacting turbulent flows with phase change due to droplet evaporation are solved on an unstructured hexahedral mesh. The droplet dynamics is modeled using the point-particle approach and a uniform state equilibrium model for evaporation. Good agreement with available experimental data for the mean and standard deviations in the velocity and droplet size throughout the domain was obtained. The only input to the simulation was the size-velocity correlations for liquid droplets at the inlet section, the mass flow rates and fluid properties. It was shown that with well prescribed boundary conditions, the present LES formulation together with the Lagrangian particle tracking captures the droplet dispersion characteristics accurately. In the present study, however, the droplet evaporation was primarily governed by mass-diffusion. The vapor mass-fractions in the surrounding fluid are considerably lower than those at the droplet surface. The influence of droplet evaporation on scalar dissipation rates and mixture fraction variance was not pronounced. The present formulation together with advanced models for micro-mixing can be used to simulate turbulent spray combustion in realistic configurations.

19

Acknowledgments

References

[1] Mahesh, K.. Constantinescu, G., and Moin, P., *J. Comp. Phy.*, 197:215–240 (2004).

[2] Elghobashi, S., *Appl. Sci. Res.* 52:309–329, (1984).

[3] Reade, W. C. and Collins, L. R. *Phys. Fluids* 12:2530–2540, (2000).

[4] Rouson, D. W. I. and Eaton, J. K. *J. Fluid Mech.* 348:149–169, (2001).

[5] Wang, Q. and Squires, K.D., *Phy. Fluids*, 8:1207–1223, (1996).

[6] Apte, S. V., Mahesh, K., Moin, P., and Oefelein, J.C., *Int. J. Mult. Flow* 29:1311–1331 (2003a).

[7] Sommerfeld, M., Ando, A., and Qiu, H. H. *J. Fluids. Engr.*, 114:648–656 (1992).

[8] Pozorski, J., and Apte, S.V.., *Int. J. Mult. Flow*, accepted pending revisions, 2008.

[9] Fede, P., Simonin, O., Villedieu, P., and Squires, K.D., *Proc. Summer Program, Center for Turbulence Research*, Stanford University, (2006).

[10] O'Kongo, N., and Bellan, J. *J. Fluid Mech*, 499:1–47, (2004)

[11] Reveillon, J., and Vervisch, L. *Comb. Flame*, 121:75–90 (2000).

[12] Apte, S. V., Gorokhovski, M., and Moin, P., *Int. J. Mult. Flow* 29:1503–1522 (2003b).

[13] Patel, N., Kirtas, M., Sankaran, V., and Menon, S, *Proc. Comb. Inst.*, 31:2327–2334 (2007).

[14] Mahesh, K., Constantinescu, G., Apte, S.V., Iaccarino, G., Ham, F., and Moin, P., *ASME J. App. Mech.*, 7:374–381 (2006).

[15] Sommerfeld, M., and Qiu, H.H., *Int. J. Heat Fluid Flow*, 19:10–22 (1998).

[16] Chen, X. Q., and Pereira, J. C. F., *Int. J. Heat Mass Transfer* 39:441 (1996).

[17] Liu, Z., Zheng, C., and Zhou, L., *Proc. Comb. Inst.* 29:561–568 (2002).

[18] Moin, P., Squires, K., Cabot, W., and Lee, S., *Phy. Fluid A.*, 3:2746–1757 (1991).

[19] Pierce, C. and Moin, P., *Phy. Fluids*, 10:2041–3044 (1998).

[20] Crowe, C., Sommerfeld, M., and Tsuji, Y. *Multiphase flows with droplets, and particles*, CRC Press (1998).

[21] Apte, S. V., Mahesh, K., and Lundgren, T., *Int. J. Mult. Flow* 34: 260–271 (2008).

[22] Faeth, G., *Prog. Energy Combust. Sci.*, 9:1–76 (1998).

[23] Law, C.K., *Prog. Energy Combust. Sci.* 8:171 (1982).

[24] Sirignano, W. M., *Fluid Dynamics and Transport of Droplets and Sprays*, Cambridge University Press, Cambridge, 1999.

[25] Miller, R., Harstad, K., and Bellan, J., *Int. J. Mult. Flow*, 24:1025–1055 (1998).

[26] Masoudi, M., and Sirignano, W.A. *Int. J. Mult. Flow*, 27: 1707–1734, 2001.

[27] Oefelein, J. C., *Simulation and analysis of turbulent multiphase combustion processes at high pressures*, Ph.D. Thesis, The Pennsylvania State University, University Park, Pa, 1997.

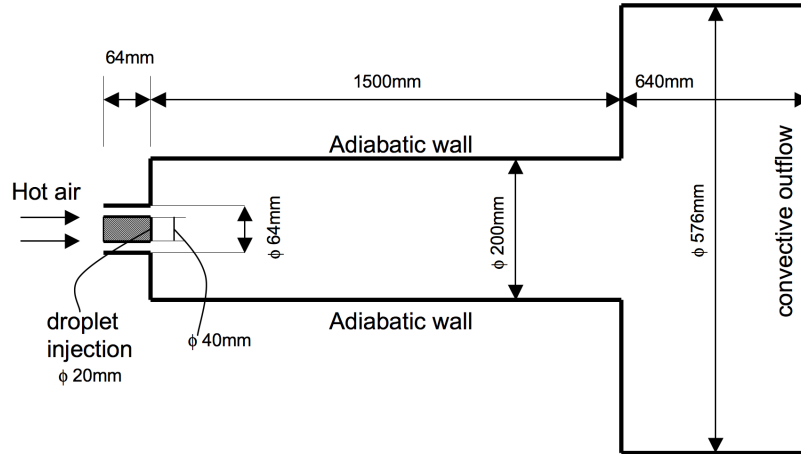[28] Pierce, C.D., and Moin, P., *AIAA J.*, 36:1325–1327 (1998).

List of Figures

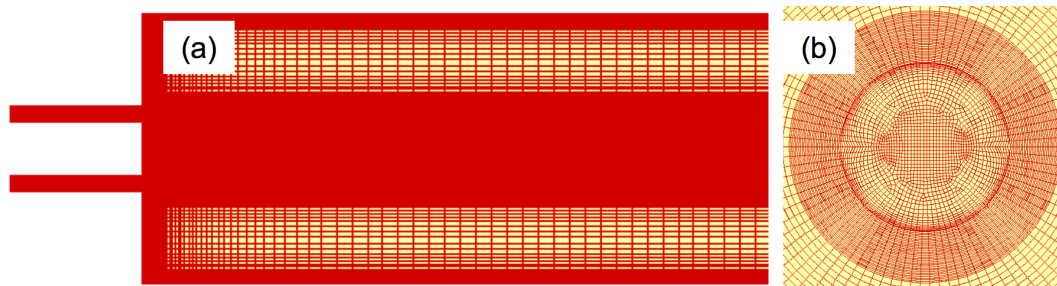Fig. 1. Schematic diagram of the computational domain for model combustor of Sommerfeld & Qiu [15].

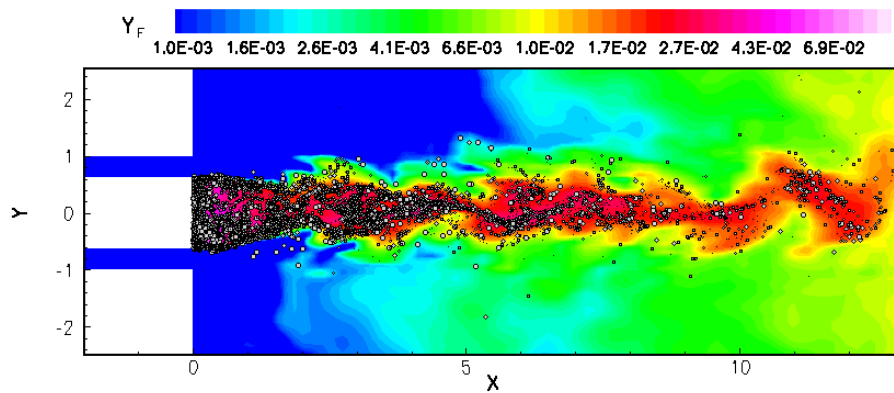Fig. 2. Close-up of the computational grid: (a) x–y plane, (b) y–z.

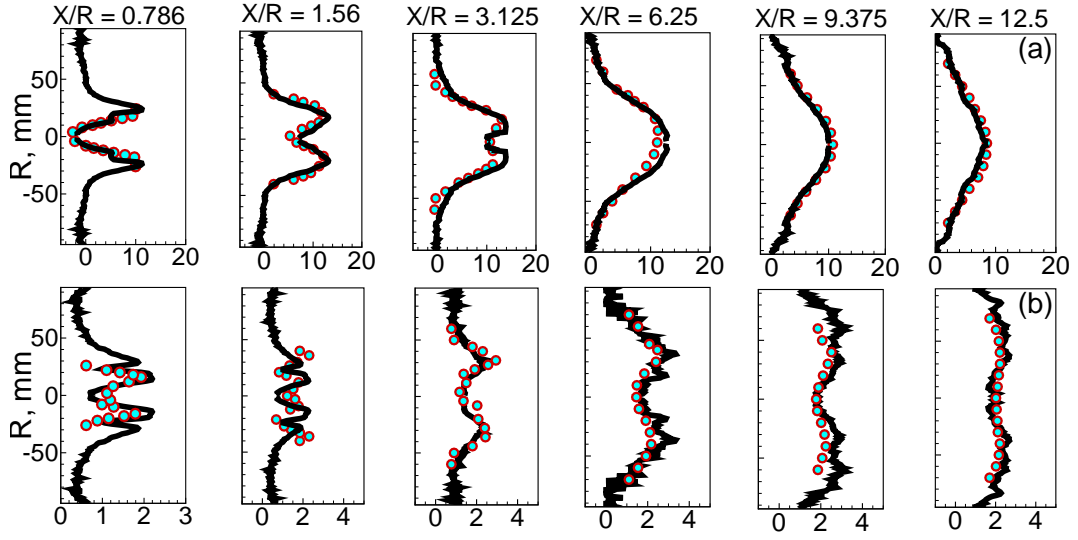Fig. 3. Instantaneous snapshot of fuel mass-fraction and liquid droplets in the z = 0 plane.

23

Fig. 4. Comparison of mean and *rms* axial velocity averaged over all droplet sizes at different axial locations: (a) $\overline{u}$, (b) u' in m/s, ∘ experiments, —— LES.
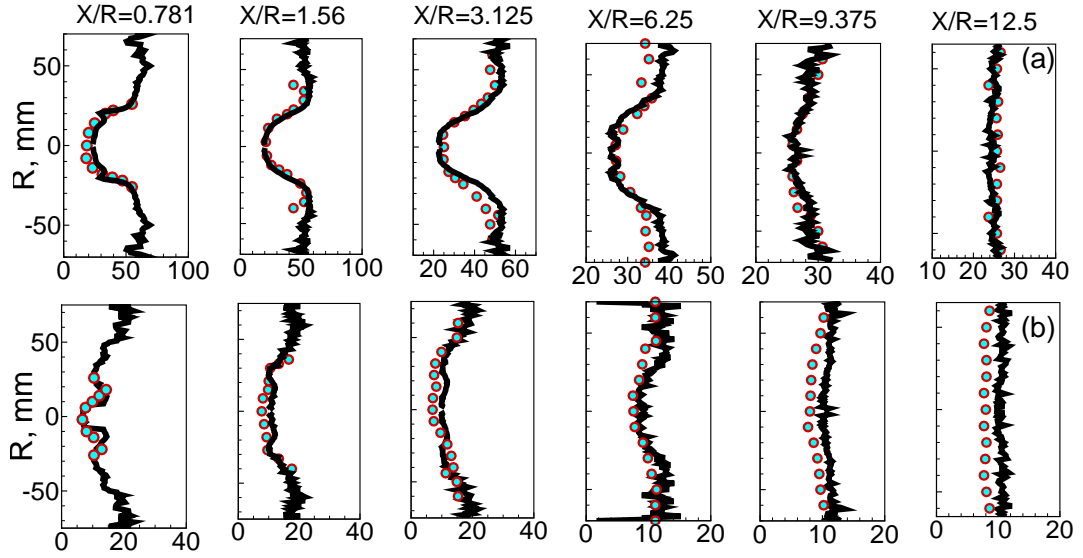

Fig. 5. Comparison of mean and *rms* droplet diameters averaged over all droplet sizes at different axial locations: (a) $\overline{d}_p$, (b) d'_p in μm, ∘ experiments, —— LES.
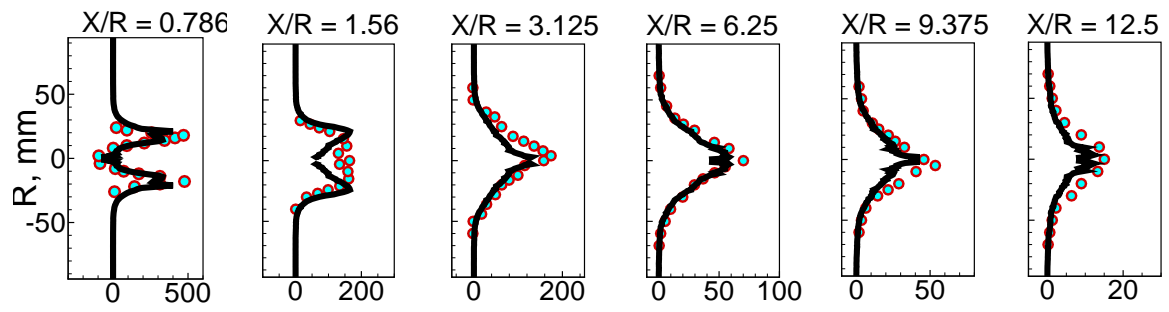
24

Fig. 6. Comparison of droplet axial mass flux (in g/m^2.s) at different axial locations, ∘ experiments, —— LES.